Theoretical Chemistry Accounts (2021) 140:29
https://doi.org/10.1007/s00214-021-02728-x

REGULAR ARTICLE

Electronic transitions in Rb_2^+ dimers solvated in helium

Simon Albertini[1] · Paul Martini[1] · Arne Schiller[1] · Harald Schöbel[1,3] · Elham Ghavidel[1] · Milan Ončák[1] · Olof Echt[1,2] · Paul Scheier[1]

Received: 1 December 2020 / Accepted: 8 February 2021 / Published online: 1 March 2021

Abstract
We have measured depletion spectra of the heteronuclear ($^{85}Rb^{87}Rb^+$) dimer cation complexed with up to 10 He atoms. Two absorption bands are observed between 920 and 250 nm. The transition into the repulsive $1^2\Sigma_u^+$ state of $HeRb_2^+$ gives rise to a broad feature at 790 nm (12,650 cm^{-1}); it exhibits a blueshift of 98 cm^{-1} per added He atom. The transition into the bound $1^2\Pi_u$ state of $HeRb_2^+$ reveals vibrational structure with a band head at $\leq$ 15,522 cm^{-1}, a harmonic constant of 26 cm^{-1}, and a spin–orbit splitting of $\leq$ 183 cm^{-1}. The band experiences an average redshift of -38 cm^{-1} per added He atom. Ab initio calculations rationalize the shape of the spectra and spectral shifts with respect to the number of helium atoms attached. For a higher number of solvating helium atoms, symmetric solvation on both ends of the Rb_2^+ ion is predicted.

Keywords Rubidium dimer ion solvated in helium · Optical spectroscopy · Excited states · Ab initio calculation · Path integral molecular dynamics (PIMD) calculations · Spin–orbit splitting

1 Introduction

Helium nanodroplets have been used as nanocryostats to isolate atoms or molecules at a temperature of 0.4 K, or to form new weakly bound aggregates [1–3]. They offer a unique quantum solvent for studying small and large dopant clusters, neutral or ionic, which can in turn be investigated by electronic or infrared spectroscopy [4]. They also minimize matrix-induced spectral shifts and broadening [5–7]. Alkali metal atoms reside on the surface of He droplets due to the short-range Pauli repulsion between their s valence electrons and surrounding helium atoms counteracting the van der Waals attractive forces [8, 9]. However, alkali metal clusters are drawn into He droplets above a critical cluster size [10–12]. By increasing the size of the alkali metal cluster, its van der Waals attraction to the helium matrix grows faster than the repulsive energies, and above a certain size it becomes favorable for clusters to submerge in the superfluid HND.

Alkali metal dimers have been investigated both experimentally [13–19] and theoretically [20–29] to provide a detailed description of the molecular electronic structure. Gabbanini produced translationally cold Rb dimers in the lowest triplet and singlet states, which were detected by resonance-enhanced photoionization [30]. Lee and Mahan have photoionized the vapor of rubidium in the discrete region of the atomic spectrum [31]. The ions produced were identified by ion mobility measurements, and a lower limit of 0.73 eV (5900 cm^{-1}) was obtained for the dissociation energy (D_e) of Rb_2^+. Olson has estimated $D_e = 0.75$ eV from the velocity dependence of the $Rb–Rb^+$ charge exchange cross section [32]. Wagner and Isenor have studied multiphoton ionization and dissociation of Rb dimers in a molecular beam; they deduced $D_e = 0.75 \pm 0.10$ eV [18].

From the theoretical viewpoint, Bellomonte et al. [33] used Hellman-type model potentials to calculate the ground-state properties of Na_2^+, K_2^+, Rb_2^+ and Cs_2^+. They reported a ground-state energy of 5.04 eV, $D_e = 0.86$ eV, equilibrium

Published as part of the special collection of articles "Festschrift in honor of Fernand Spiegelmann".

✉ Milan Ončák
Milan.Oncak@uibk.ac.at

✉ Olof Echt
Olof.Echt@unh.edu

[1] Institut für Ionenphysik und Angewandte Physik, Universität Innsbruck, 6020 Innsbruck, Austria

[2] Department of Physics, University of New Hampshire, Durham, NH 03824, USA

[3] Present Address: Department Biotechnology & Food Engineering, Management Center Innsbruck, Innsbruck, Austria

distance (R_e) of 4.45 Å, and harmonic constant (ω_e) of 41 cm^{-1} for Rb_2^+. Jraij et al. [34] performed ab initio calculations involving non-empirical pseudopotentials, core polarization potentials and semiempirical spin–orbit pseudopotentials to calculate the ground state as well as 25 excited states of Rb_2^+ for a large range of internuclear distances. Aymar et al. [35] computed the adiabatic potential energy curves associated with dimer cations Rb_2^+, Cs_2^+ and $RbCs^+$ for the lowest eight $^2\Sigma_{g,u}$ states using either the Klapisch model potential [36] or an approach based on pseudopotentials, with the aim of analyzing the abilities and limits of the Klapisch model potentials for handling heavy molecular systems with one valence electron. More recently, Smialkowski et al. [37] applied the coupled cluster method to ionic metal dimers and trimers. They investigated the ground-state electronic structure of singly-charged molecular ions, including Rb_2^+. They obtained $R_e = 4.82$ Å, $D_e = 6151$ cm^{-1} and $\omega_e = 46.0$ cm^{-1}. Several other theoretical investigations of Rb_2^+ have been published [38–41].

Limited experimental information pertaining to electronically excited states of Rb_2^+ has been obtained from studying the effect of cooling light on the lifetime of Rb_2^+ in a magneto-optical trap [42], and from photoabsorption spectra of dense rubidium vapor [43]. Also relevant is a report by Helm et al. who have studied vibrational levels in the $1^2\Pi_u$ state of Cs_2^+ by monitoring Cs^+ photofragments resulting from absorption of laser radiation by the $^2\Sigma_g^+$ state [44]. They deduced a SO splitting of 280 ± 20 cm^{-1} in the $1^2\Pi_u$ state. We have recently studied Cs_2^+ complexed with up to 12 He atoms by depletion spectroscopy [45]. Three absorption bands were observed due to transitions from the ground state into the $1^2\Sigma_u^+$, $1^2\Pi_u$ and $2^2\Pi_u$ states. The bound $^2\Pi_u$ states in $HeCs_2^+$ were SO split by about 315 and 340 cm^{-1}, respectively.

Here, we report depletion spectra of Rb_2^+ complexed with up to ten He atoms. The ions were formed by doping helium nanodroplets in a pickup cell filled with low-density Rb vapor and subsequent electron ionization. The weak binding between He and Rb_2^+ ensures that the target ions are in their vibrational ground states. Two absorption bands are observed between 920 and 250 nm, due to transitions into the $1^2\Sigma_u^+$ and $1^2\Pi_u$ states. The transitions are blue- and redshifted, respectively, when the number of He atoms is increased. Spectroscopic constants and the spin–orbit (SO) splitting are deduced for the bound $1^2\Pi_u$ state. All experimental findings are supported by ab initio calculations.

2 Experiment

Helium nanodroplets (HNDs) were formed by supersonic expansion through a 5-µm-diameter nozzle into vacuum. The nozzle temperature ranged from 9.6 to 9.85 K for the various spectral scans. The HNDs were doped in a pickup cell filled with Rb at a temperature of 329 K which corresponds to a vapor pressure of 0.0005 Pa [46]. The doped HNDs were ionized by electrons at about 100 eV and an emission current ranging from 300 to 600 µA. $He_nRb_m^+$ ions ejected from the large multiply charged droplets were deflected by 90° via electrostatic lenses. The ion beam was guided into the extraction region of a high-resolution time-of-flight mass spectrometer (TOFMS) where it was merged with a laser beam from a tunable light source (EKSPLA NT242, line width 5 cm^{-1}, pulse duration 3–6 ns, repetition rate 1 kHz). The laser was calibrated with a spectrometer using an echelle diffraction grating (model SHR, Solar Laser Systems); the wavelength accuracy in the relevant range was 0.05 nm. The TOFMS was operated at 10 kHz, enabling simultaneous measurement of laser-on and laser-off mass spectra. Depletion spectra were extracted from the stored data for $He_n{}^{85}Rb^{87}Rb^+$ by setting a digital mass filter to ± 0.10 u within the expected mass, for each size $1 \le n \le 10$. Data for homonuclear species $He_n{}^{85}Rb_2^+$ and $He_n{}^{87}Rb_2^+$ could not be extracted because their masses coincide with those of $He_{n-1}{}^{87}Rb_2^+$ and $He_{n+1}{}^{85}Rb_2^+$, respectively. Representative mass spectra are provided in the Electronic Supplementary Information (ESI). Depletion spectra are corrected for the wavelength-dependent output power of the laser. Conversion from wavelengths to energies takes into account the refractive index of air ($n = 1.000293$). A detailed description of the experiment has been given in the ESI of Ref. [45].

3 Calculations

For modeling the ground electronic state, we used the coupled clusters singles doubles (CCSD) method. For electronically excited states, the equation of motion CCSD (EOMCSD) [47–49] and multireference configuration interaction (MRCI) [50, 51] were employed. We used various basis sets from the def2 series (def2TZVP, def2QZVP, def2QZVPPD) as well as the Stuttgart basis set ECP28MDF [52] for modeling spin–orbit coupling; basis set benchmarking is available as Table S1 in the ESI. In all used basis sets, 17 electrons of Rb_2^+ are treated explicitly; the remaining ones are included in the effective core potential (ECP). For optimization of the $He_nRb_2^+$ clusters, tight optimization criteria were used to describe the very floppy potential energy surface. Zero-point energy correction was accounted for in all reported thermochemical values.

Within the (EOM)CCSD calculations, we used either one explicitly correlated electron of Rb_2^+ (corresponding to the frozen core, FC, approximation) or we correlated all Rb electrons; all He electrons were always correlated. The frozen core approximation is obviously advantageous for reaching the goal of the present study, i.e., modeling

weakly bound $He_nRb_2^+$ clusters, $n \leq 10$, leading to a decrease in the computational time. The difference between both approaches is most visible for the Rb–Rb bond length, predicting 5.185 and 4.883 Å with frozen core approximation and when correlating all electrons, respectively, within the CCSD/def2QZVPPD method. Photochemical properties are somewhat less influenced, with 1.57 and 1.52 eV for excitation into the $^2\Sigma_u^+$ state and 1.83 and 1.98 eV into the $^2\Pi_u$ state within the EOMCCSD/def2QZVPPD approach. Most importantly, both approaches predict the same trends with respect to shifts induced by helium solvation, which is the main concern of the present publication, and we thus use the frozen core approximation for treating clusters with larger numbers of helium atoms.

For Rb_2^+, the MRCI calculation was performed with an active space of 17 electrons in 13 orbitals, further denoted as (17,13). For $HeRb_2^+$ and $He_2Rb_2^+$, active spaces of (15,11) and (17,12) were used, respectively. The spin–orbit coupling was calculated using the state-interacting method as implemented in Molpro [53]. The SO splitting of the $1^2\Pi_u$ state in Rb_2^+ does not change considerably (<2 cm^{-1}) when switching the active space from (1,15) to (1,4) within the MRCI method. Using (17,13) active space, however, the SO splitting increases by about 15 cm^{-1}. Using the all-electron Sapporo-QZP-2012 basis set [54] shifts the splitting by less than 1% within the MRCI(17,13) method. Benchmark calculations on the Rb atom show that for the MRCI(9,12)/ECP-28MDF method, the calculated SO splitting of the 1^2P state (198 cm^{-1}) is underestimated by about 16% with respect to the experimental value (238 cm^{-1}) [55]. The reported SO splitting for Rb_2^+ could thus be underestimated. When calculating the energy of the 0–0 transition and modeling spectra of the $1^2\Pi_u$ state in the $HeRb_2^+$ and $He_2Rb_2^+$ clusters, only the Rb_2^+ vibration was included into the zero-point energy correction.

Path integral molecular dynamics (PIMD) calculations were performed on the MP2(FC)/def2QZVP(Rb),def2TZVP(He) potential energy surface; this approach was selected as a method that can be used for PIMD simulations of Rb_2^+ solvated by more He atoms in the future. Sixteen random walkers, time step of 30 a.u. and Nosé–Hoover thermostat with four chains were used. In total, 15,500 steps were calculated, with 5000 initial steps used as a thermalization period. A temperature of 5 K was used for efficient sampling. Out of the trajectory, 1730 structures were used for spectrum modeling within the reflection principle [56–58], and calculated points were convoluted with Gaussian functions with full width at half maximum (FWHM) of 0.03 eV.

(EOM)CCSD and density functional theory (DFT) calculations were performed in the Gaussian software [59], and MRCI calculations in the Molpro program. PIMD simulations were performed in the *Abin* program [60]; vibrationally resolved electronic spectra were modeled within the PGOPHER software [61].

4 Results and discussion

4.1 Rb_2^+

Before discussing Rb_2^+ solvated by helium atoms, let us turn our attention to the properties of Rb_2^+ itself (Table 1). For the minimum-energy structure in the ground electronic state of $1^2\Sigma_g^+$, our calculations predict the bond length of 4.883 Å, the vibrational frequency within harmonic approximation of 44.7 cm^{-1} and dissociation energy of 5992 cm^{-1} (CCSD/def2QZVPPD), close to previous experimental and computational values. In the Franck–Condon region, there are nine excited states lying within 35,000 cm^{-1} (Fig. 1). Only transitions to states of $^2\Sigma_u^+$ and $^2\Pi_u$ character are bright ones; other transitions are forbidden. However, only the first two electronic states, $1^2\Sigma_u^+$ and $1^2\Pi_u$, have a considerable oscillator strength. Compared to the case of Cs_2^+ [45], the $2^2\Pi_u$ state has a lower transition dipole moment and is therefore not observed in the present experiment (see also below).

Focusing on the two lowest electronic states, the $1^2\Sigma_u^+$ state is dissociative due to the excitation of σ–σ* character (Fig. 2) and converges in the dissociation limit with $1^2\Sigma_g^+$. We predict the excitation energy from the minimum of the ground state as 12,290 cm^{-1}, close to the previously reported value of 12,690 cm^{-1} [34]. Note that the $1^2\Sigma_u^+$ potential is steep (Fig. 1) and already for a bond length shorter by 0.05 Å with respect to the equilibrium value, the excitation energy increases by 180 cm^{-1}. The transition is very intense, with the oscillator strength of 0.37.

The $1^2\Pi_u$ state is bound and has the equilibrium bond length of 5.455 Å (EOMCCSD/def2QZVPPD), about 0.6 Å longer than in the electronic ground state, with the calculated vibrational frequency of 25.1 cm^{-1}. The potential energy surface is shallow, and a small change in the basis set can shift the equilibrium position considerably: When the def2QZVP basis set is used, the bond length of 5.697 Å is retrieved (see Table S1). Due to the same reason, the calculated bond prolongation with respect to the ground state is about twice as large as predicted previously [34] (see also below). In this state, the odd electron is localized in a π orbital (Fig. 2). The vertical excitation energy is calculated as 15,990 cm^{-1}; the energy difference between $1^2\Sigma_g^+$ and $1^2\Pi_u$ minima including the zero-point correction is 15820 cm^{-1}. This is virtually the same value as reported previously, 15,870 cm^{-1} [34]. Again, the transition is considerably intense, with the oscillator strength of 0.29 for each branch of the $1^2\Pi_u$ state.

While there is only a negligible shift due to spin–orbit interaction for the $1^2\Sigma_g^+$ state (<0.1 cm^{-1}), the $1^2\Pi_u$ state

Table 1 Properties of Rb_2^+, $HeRb_2^+$ and $He_2Rb_2^+$ in the $1^2\Sigma_g^+$ electronic ground state, $1^2\Sigma_u^+$ state and spin–orbit (SO) split $1^2\Pi_u$: Equilibrium Rb–Rb internuclear distance, dissociation energies (D_e or D_0), harmonic constant ω_e for the Rb–Rb stretch and transition energies (T_e and T_0 for $1^2\Sigma_u^+$ and $1^2\Pi_u$, respectively)

Ion	State	Method	R_e [Å]	D_e or D_0 [cm^{-1}]	ω_e [cm^{-1}]	T_e or T_0 [cm^{-1}]
Rb_2^+	$1^2\Sigma_g^+$	Exp	–	≥5900[a], 6050[b], 6050 ± 810[c]	–	–
		Theory	4.883; 4.82[d]; 4.79[e]	5992; 6151[d]	44.7; 46.0[d]; 45.96[e]	–
	$1^2\Sigma_u^+$	Theory	Unbound	–	–	12,290; 12,690[e]
	$1^2\Pi_u$ 1/2	Theory	5.455[f]; 5.12[e]	–	25.1[f]; 28.59[e,f]	15,770; 15,795[e]
	$1^2\Pi_u$ 3/2	Theory	5.455[f]; 5.09[e]	–	25.1[f]; 28.59[e,f]	15,880; 15,937[e]
$HeRb_2^+$	$1^2\Sigma_g^+$	Theory	4.889	5916[g]	43.2	–
	$1^2\Sigma_u^+$	Exp.[h]	–	–	–	12,652 ± 16
		Theory	Unbound	–	–	12,500
	$1^2\Pi_u$ 1/2	exp.[i]	–	–	25.90 ± 0.07	≤ 15,522 ± 3
		Theory	5.452[f]	–	25.0[f]	15,680
	$1^2\Pi_u$ 3/2	Exp.[i]	–	–	25.68 ± 0.06	≤ 15,705 ± 3
		Theory	5.452[f]	–	25.0[f]	15,800
$He_2Rb_2^+$	$1^2\Sigma_g^+$	Theory	4.891	5848[g]	41.5	–
	$1^2\Sigma_u^+$	Exp.[h]	–	–	–	12,779 ± 20
		Theory	Unbound	–	–	12,730
	$1^2\Pi_u$ 1/2	Exp.[i]	–	–	26.03 ± 0.04	≤ 15,464 ± 3
		Theory	5.448[f]	–	24.9[f]	15,600
	$1^2\Pi_u$ 3/2	Exp.[i]	–	–	26.03 ± 0.04	–
		Theory	5.448[f]	–	24.9[f]	15,710

Unless noted otherwise, calculations stem from the current study and were performed at the (EOM)CCSD/def2QZVPPD level of theory spin–orbit coupling was calculated at the MRCI/ECP28MDF(Rb),def2TZVP(He) level. (See the Calculations section for active space definition.) Calculated excitation energies are rounded to 10 cm^{-1}

[a][31]

[b][32]

[c][18]

[d][37]

[e][34]

[f]computed without spin–orbit coupling

[g]dissociation energy with helium atoms staying on Rb^+

[h]this work, midpoint of absorption band, for $He_n{}^{85}Rb^{87}Rb^+$; see text for details

[i]this work, band heads for $He_n{}^{85}Rb^{87}Rb^+$; see text for details

splits considerably, with the gap between the resulting Ω = 1/2 and Ω = 3/2 states calculated as 111 cm^{-1} for the minimum structure (MRCI(17,13)/ECP28MDF), in reasonable agreement with 142 cm^{-1} predicted previously [34].

Two other bright states, $2^2\Sigma_u^+$ and $2^2\Pi_u$, are predicted to lie at about 32,000 cm^{-1} (Fig. 1). Both are dissociative within the considered Rb–Rb length range and have oscillator strengths below 0.015. At the same time, they have not been observed experimentally so far. Therefore, they are not discussed here further.

4.2 $HeRb_2^+$ and $He_2Rb_2^+$

Measured depletion spectra of $^{85}Rb^{87}Rb^+$ complexed with n = 1, 2, 3, 6 and 9 He atoms are displayed in Fig. 3. Data from two separate scans have been combined, one ranging from 600 to 700 nm in 0.1 nm increments and the other from 700 to 920 nm in 0.2 nm increments. The dwell time was 60 s per step. The data shown were averaged over 10 adjacent points in order to reduce statistical scatter.

Two absorption bands are shown in Fig. 3 for $HeRb_2^+$, a broad one at about 12,700 cm^{-1} and a narrow one at about 15,700 cm^{-1}. For $He_2Rb_2^+$, the transitions are slightly blue- and redshifted, respectively. Based on previous theoretical calculations on Rb_2^+ and potential energy curves in Fig. 1, we assign these states as transitions from the $1^2\Sigma_g^+$ ground state into the $1^2\Sigma_u^+$ and $1^2\Pi_u$ states, respectively. Their centroids have been determined by fitting Gaussians (for the $1^2\Sigma_u^+$ state) or square functions (for the $1^2\Pi_u$ state); the results are represented in Fig. 3 by solid (red) lines.

When one helium atom is attached to the Rb_2^+ ion, a linear structure is obtained (Fig. 4), with the Rb–He

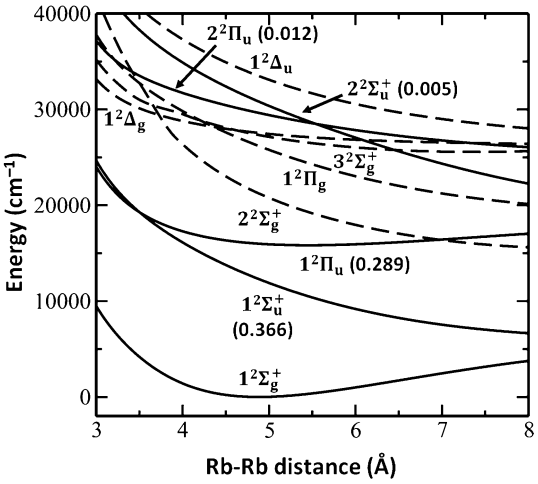

Fig. 1 Electronic states in Rb_2^+ calculated at the (EOM)CCSD/def2QZVPPD level. Bright and forbidden states are shown as full and dashed lines, respectively. Oscillator strengths for bright states are given in parentheses as calculated at the bond length of 4.883 Å

distance of 3.435 Å. The Rb–Rb bond is mildly affected by the presence of the helium atom, shifting by less than 0.01 Å (CCSD/def2QZVPPD). The adsorption energy of the helium atom is predicted as 26 cm^{-1} at this level of theory; the helium atom can roam freely around the Rb_2^+ core starting with 23 cm^{-1} of kinetic energy. (See the transition state structure in Fig. 4.) In the $1^2\Pi_u$ state, the linear structure is slightly distorted, the Rb–Rb bond distance increases considerably to 5.452 Å, and the Rb–He distance shrinks to 3.138 Å. This change can be understood based on the Pauli repulsion (Fig. 2). In the ground state, the helium atom is slightly repelled by the σ orbital. In the excited state, He can position itself closer to Rb_2^+ due to the shape of the π orbital. Structures calculated for $He_2Rb_2^+$ show the same trends as for $HeRb_2^+$. However, two isomers are retrieved here (Fig. 4b), with both helium atoms on the one side (**IIa**) or distributed equally (**IIb**).

The structureless band observed for the $1^2\Sigma_u^+$ state in Fig. 3 reflects the dissociative nature of this electronic state. In $HeRb_2^+$, it has an experimental FWHM of 1200 cm^{-1}. The spectrum modeled from the ground-state density sampled by path integral molecular dynamics on the MP2(FC)/def2QZVP(Rb),def2TZP(He) potential energy surface at the temperature of 5 K is also shown. Here, the FWHM is estimated as 900 cm^{-1}, slightly underestimating the experimental width, but still reproducing the measured spectrum well. The agreement in the spectral position is fortuitous given approximations included.

The transition into the bound $1^2\Pi_u$ state reveals vibrational structure. Depletion spectra recorded with 0.1 nm increments and a dwell time of 180 s per data point are displayed in Fig. 5 for $HeRb_2^+$ and $He_2Rb_2^+$. For $HeRb_2^+$, the envelope of the curve suggests that we are seeing the superposition of two vibrational progressions, due to transitions into the Ω = 1/2 and 3/2 components of the SO split $^2\Pi_u$ state. The vertical lines in Fig. 5a mark possible candidates for the (*v*', *v*'') = (0,0) transitions at 15,522 cm^{-1} and 15,705 cm^{-1}. They would imply a SO splitting of 183 cm^{-1}, compared with a theoretical value of 116 cm^{-1}

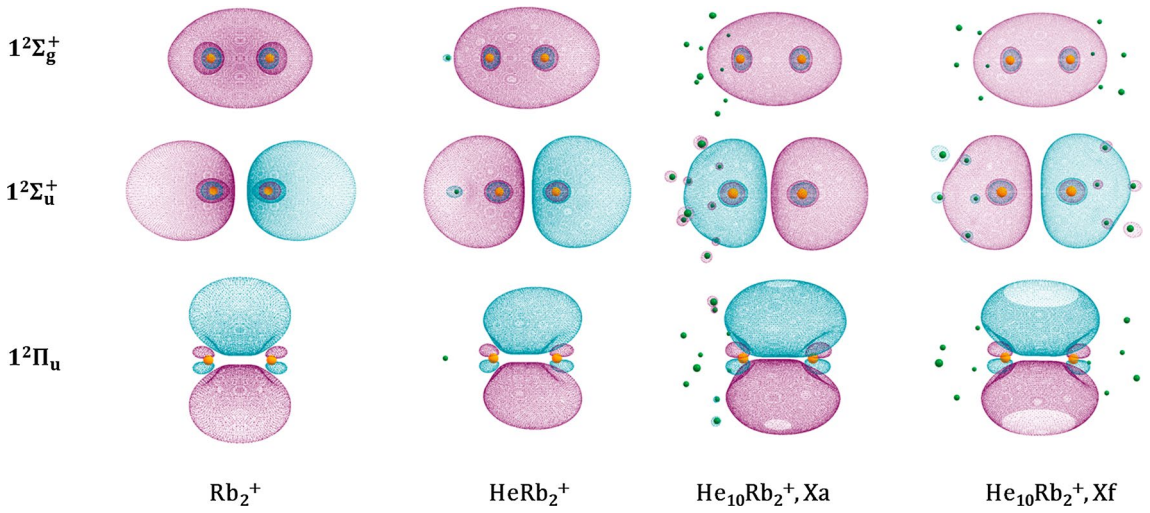

Fig. 2 Molecular orbitals in which the sole electron is localized in three lowest electronic states of Rb_2^+, $HeRb_2^+$, and two isomers of $He_{10}Rb_2^+$. Calculated at the CAM-B3LYP/def2QZVPPD level of theory. Note that a low contour value was chosen as to display the relatively small influence of helium on the electronic structure of Rb_2^+

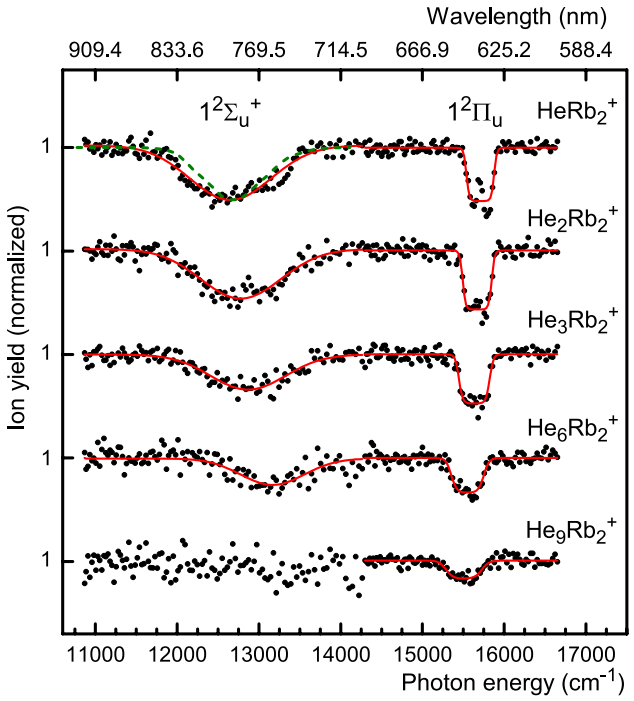

Fig. 3 Low-resolution depletion spectra of $^{85}Rb^{87}Rb^+$ complexed with $n = 1$, 2, 3, 6 and 9 He atoms. The solid (red) lines represent fits to the absorption bands that are due to transitions into the $1^2\Sigma_u^+$ and $1^2\Pi_u$ states. The dashed (olive) line is the calculated spectrum modeled at the EOMCCSD(FC)/def2QZVPPD level on structures sampled from the PIMD on the MP2(FC)/def2QZVP(Rb),def2TZVP(He) potential energy surface (see text for details)

for $HeRb_2^+$ (this work) and of 142 cm^{-1} for Rb_2^+ [34]. As discussed in the Calculations section, our results probably underestimate the real value.

The data in Fig. 5a were analyzed by fitting two sets of equidistant Lorentzians with spacing ω_1 and ω_2, respectively. Results are compiled in Table 1. The fitted vibrational constants, 25.9 and 25.7 cm^{-1} for the 1/2 and 3/2 states, respectively, are in agreement with 25.0 cm^{-1} for $HeRb_2^+$ (this work) and 28.59 cm^{-1} for Rb_2^+ [34] computed for the $1^2\Pi_u$ state in the absence of SO coupling.

The depletion spectrum of $He_2Rb_2^+$ (Fig. 5b) is qualitatively similar to that of $HeRb_2^+$. A single progression of 15 equally spaced Lorentzians was fit to the data, resulting in a harmonic constant $\omega_e = 26.03 \pm 0.02$ cm^{-1} (Fig. 5b). It is not possible to identify the (0,0) origin of the progression, but the envelope is clearly shifted to lower energies with respect to $HeRb_2^+$.

There is no evidence for anharmonicity in the observed vibrational progressions. This is not surprising because the ratio of the anharmonic to the harmonic constants, $\omega_e x_e/\omega_e$ (calculated for the ground state whose values of R_e and D_e are quite similar to those of the $^2\Pi_u$ state), is only 0.2% [39]. Perhaps, more surprising is the absence of a phase shift between the two overlapping progressions, which must be accidental.

As shown in Fig. 1, the calculated equilibrium distance in the $1^2\Pi_u$ state exceeds that in the ground state, and the (0,0) transition may well be unobservable. On the other hand, the

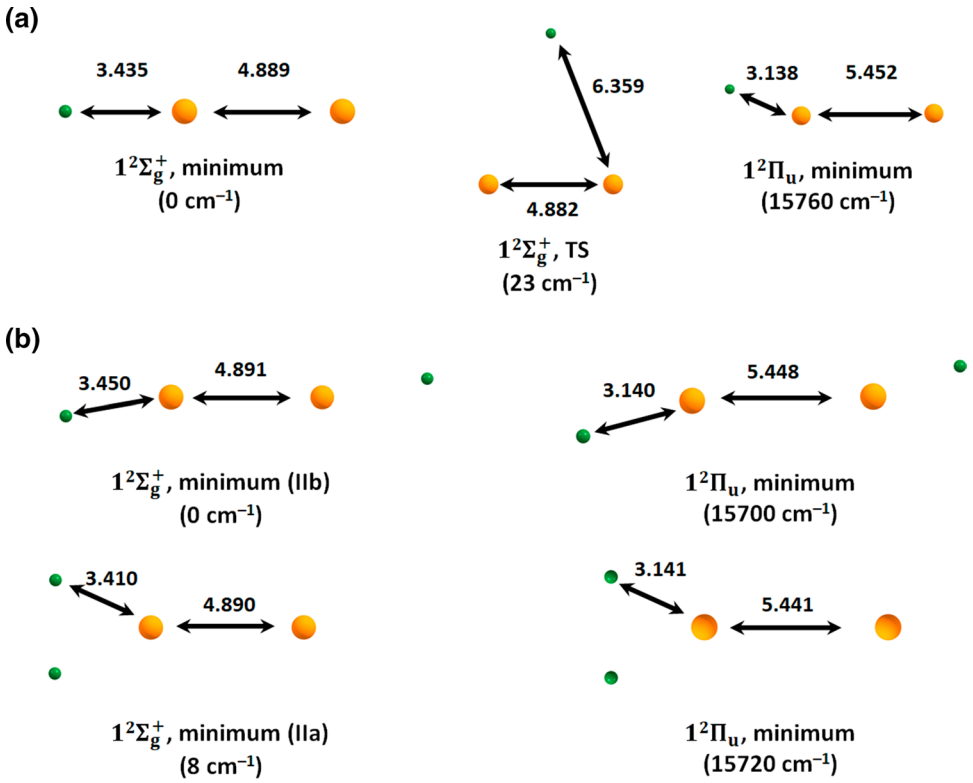

Fig. 4 **a** Structures of $HeRb_2^+$ for the equilibrium in the $1^2\Sigma_g^+$ and $1^2\Pi_u$ states and the transition state for helium moving to the other side of Rb_2^+ in the $1^2\Sigma_g^+$ state, **b** structures of two isomers of $He_2Rb_2^+$ for the equilibrium in the $1^2\Sigma_g^+$ and $1^2\Pi_u$ states. Relative energies of isomers and bond lengths (in Å) are given. Calculated at the (EOM)CCSD/def2QZVPPD level of theory

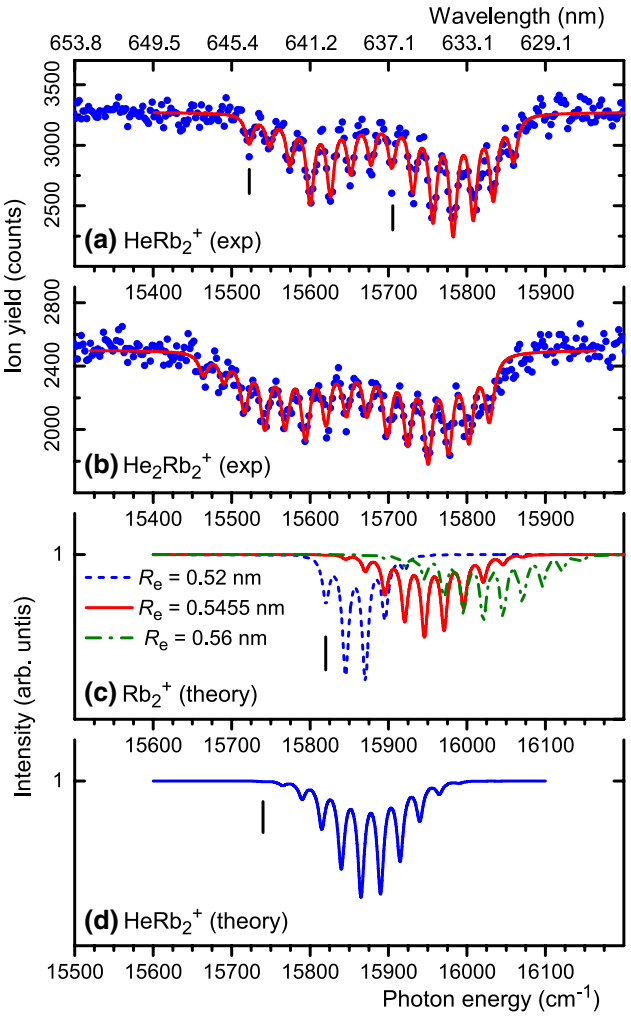

Fig. 5 **a**, **b** High-resolution depletion spectra of heteronuclear Rb_2^+ complexed with one or two He atoms. The data reveal two overlapping vibrational progressions for transitions into the spin–orbit split $1^2\Pi_u$ state. The red solid lines represent fits of two sets of equally spaced Lorentzians to the experimental data. **c** Modeled depletion spectra of Rb_2^+ for different equilibrium distances in the $1^2\Pi_u$ state (without SO coupling), with other parameters calculated at the (EOM)CCSD/def2QZVPPD level. The harmonic vibrational frequency was kept constant as calculated in the minimum (25.1 cm^{-1}); Lorentzian broadening of 10 cm^{-1} was employed. The vertical line indicates the (0,0) transition. **d** Modeled depletion spectrum of $HeRb_2^+$ calculated at the (EOM)CCSD/def2QZVPPD level

equilibrium bond length in the $1^2\Pi_u$ state varies greatly at different levels of theory due to a floppy potential. In Fig. 5c, we show depletion spectra of Rb_2^+ simulated for three different Rb–Rb distances in the $1^2\Pi_u$ state in the absence of SO coupling. (Note that the *x*-axis has been shifted in order to facilitate a comparison with the experimental data.) For the Rb–Rb distance of 5.2 Å, there are only five clear bands predicted. The (0,0) transition (marked by a vertical line) has a large Franck–Condon factor, and the (0,2) transition is the most intense one. For $R_e = 5.455$ Å (the equilibrium distance calculated at the (EOM)CCSD/def2QZVPPD level), a larger number of intense transitions are observed, with the most intense one being (0,5). Finally, for $R_e = 5.6$ Å, the maximum shifts to (0,8) and even more bands are seen. In Fig. 5d, the computed spectrum for the equilibrium structure of $HeRb_2^+$ is shown, which is very similar to the one for Rb_2^+. Compared to the experimental data, we can conclude that the modeled spectrum for the Rb–Rb distance of ~ 5.45 Å reproduces the data reasonably well, although one cannot exclude that the Rb–Rb distance for the $1^2\Pi_u$ state is somewhat longer. This would imply that the (0,0) transition is not observed in the experiment, and the energies of the transitions into the SO split $1^2\Pi_u$ ($v' = 0$) state are smaller than the upper limits listed in Table 1 by a few vibrational quanta.

Finally, we analyze spectral shifts induced by the presence of a helium atom. As can be seen in Table 1, the $1^2\Sigma_g^+$–$1^2\Sigma_u^+$ transition is predicted to shift to a higher energy by 210 cm^{-1} and the $1^2\Sigma_g^+$–$1^2\Pi_u$ transition shifts down by either 60 cm^{-1} (for vertical excitation energies in the respective minima) or 90 cm^{-1} (for the (0,0) transition) between Rb_2^+ and $HeRb_2^+$. These shifts can be qualitatively understood by inspection of molecular orbitals depicted in Fig. 2 (see also Ref. [45]): The $1^2\Sigma_g^+$ ground state is slightly destabilized by the presence of the helium atom; this destabilization, however, increases in the $1^2\Sigma_u^+$ state. In the $1^2\Pi_u$ state, on the other hand, the Pauli repulsion with helium is reduced as the molecular orbital does not extend along the Rb–Rb axis. Thus, there is a considerable shift to higher excitation energies for the $1^2\Sigma_g^+$–$1^2\Sigma_u^+$ transition due to the destabilization of the target state. For the $1^2\Sigma_g^+$–$1^2\Pi_u$ transition, the destabilization in the $1^2\Sigma_g^+$ state prevails, leading to a smaller negative shift.

For the difference between $HeRb_2^+$ and $He_2Rb_2^+$, we obtain similar spectral shifts of 230 cm^{-1} and –80 cm^{-1} for the $1^2\Sigma_g^+$–$1^2\Sigma_u^+$ and $1^2\Sigma_g^+$–$1^2\Pi_u$ transitions, respectively. Here, we can directly compare these values with the experimental ones of 127 ± 26 cm^{-1} and -58 ± 5 cm^{-1} (Table 1). The considerable discrepancy for the shift of the $1^2\Sigma_g^+$–$1^2\Sigma_u^+$ state can be most probably traced to the floppy potential energy surface with respect to the helium position. For example, an increase of 0.3 Å in the Rb–He distance leads to the change in the ground-state energy by 7 and 13 cm^{-1} for $HeRb_2^+$ and $He_2Rb_2^+$, respectively. However, the spectral shift of the $1^2\Sigma_g^+$–$1^2\Sigma_u^+$ transition decreases to 151 cm^{-1} for these structures, i.e., to about 60% of the one for minimum energy structures. The modeled shifts can thus be easily influenced by small changes in the methodology (e.g., inclusion of triples within the CC formalism) as well

as by inclusion of dynamic effects and cannot be interpreted quantitatively.

4.3 $He_nRb_2^+$, $n = 3–10$

Let us now turn to clusters solvated with several helium atoms. A vibrational progression is still discernible for $He_3Rb_2^+$ (see Fig. S3 of the ESI); its envelope is redshifted even further. Vibrationally unresolved depletion spectra were recorded for even larger $He_nRb_2^+$, $n \leq 10$; square functions were fitted to the absorption bands in order to deduce the spectral shift.

The midpoints of the absorption bands *versus* the number n of attached He atoms are compiled in Fig. 6. Data for $He_4{}^{85}Rb^{87}Rb^+$ could not be deduced because its mass coincides with that of impurity ions, $H_2O^{85}Rb_2^+$ and $O^{85}Rb^{87}Rb^+$. The transition to the $1^2\Sigma_u^+$ state is blueshifted with increasing size n by $+98 \pm 6$ cm^{-1} per added He atom (the dashed line represents the result of a fit to the data). The transition to the $1^2\Pi_u$ state is redshifted, on average, by -38 ± 3 cm^{-1} for the first five He atoms but gradually tapers off. The total redshift between $n = 1$ and $n = 10$ equals about –210 cm^{-1}.

Selected calculated structures of $He_nRb_2^+$, $n = 2–10$, are shown in Fig. 7 (see the ESI for all isomers); their properties are collected in Table 2. Note that for these larger clusters, we used the frozen core approximation, leading among other effects to prediction of linear isomer **IIb**. The **a**, **b**, **c**… nomenclature follows the distribution of He atoms on both sides of Rb_2^+, from the most asymmetric one to more equal ones. Although the calculated structures necessarily represent only a subset of all possible local minima, several trends are clearly visible. Most importantly, isomers with all helium atoms on the one side (**a** isomers) are usually the least stable ones and exhibit the lowest absolute value of spectral shifts. This can be documented on the spectral shift for the $1^2\Sigma_g^+–1^2\Pi_u$ transition where even positive shifts are observed (**Xa**). Structures with a similar number of helium atoms on each side, on the other hand, exhibit higher stability and more considerable spectral shifts. Again, this can be understood based on the molecular orbital picture (Fig. 2). For more helium atoms on the one side (**Xa**), the molecular orbital might deform toward the other side to compensate the Pauli repulsion. For equal distribution of helium atoms on both sides (**Xf**), the orbital is more constricted, leading to a more considerable shift. Within the CCSD(FC) method, the Rb–Rb bond length decreases by 0.006 Å when passing from Rb_2^+ to $He_nRb_2^+$, $n = 6$, and by another 0.002 Å between $n = 6$ and $n = 10$ (for the most stable isomers in Table 2).

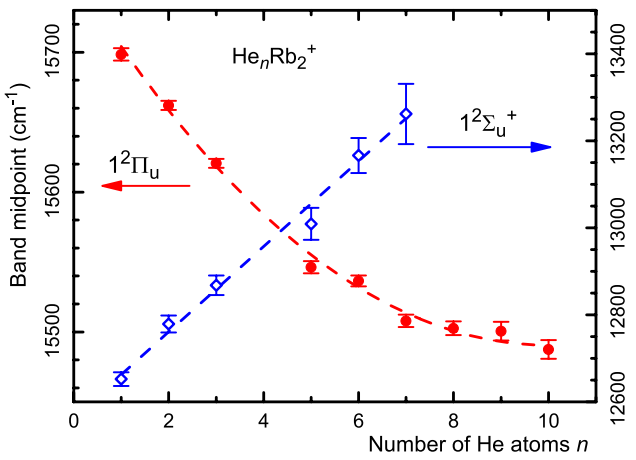

Fig. 6 The centroids of the absorption bands in Fig. 3 versus the number n of He atoms attached to the heteronuclear Rb_2^+ dimer. Transitions into the $1^2\Sigma_u^+$ state (right scale) are blueshifted with increasing n, while transitions into the $1^2\Pi_u$ state (left scale) are redshifted

The calculated shifts for the $1^2\Sigma_g^+–1^2\Sigma_u^+$ transition in Table 2 reproduce the experimental trend (Fig. 6) quantitatively. However, this is probably due to error compensation as correlation of all electrons leads to a shift that is considerably larger. (See Table 1 and the discussion above.) The shifts for the $1^2\Sigma_g^+–1^2\Pi_u$ transition, on the other hand, are considerably underestimated. Here, however, the values presented in Table 2 were calculated for the vertical transition from the minimum. If we account for relaxation in the target state, higher absolute shifts may be expected.

Overall, both thermochemical and photochemical data show that for the Rb_2^+ solvated by helium atoms, symmetric solvation is the most probable one, as already observed for a low number of helium atoms in lighter alkali dimer ions [62]. This trend can be expected to continue until the first solvation layer is filled.

5 Conclusions

In Rb_2^+ solvated by helium atoms, only two electronic transitions are observed experimentally, $1^2\Sigma_g^+–1^2\Sigma_u^+$ and $1^2\Sigma_g^+–1^2\Pi_u$. The $1^2\Sigma_u^+$ state is repulsive and shifts to higher energies with helium solvation because helium atoms deform the target σ* orbital more considerably compared to the σ orbital in the ground state. In the $1^2\Pi_u$ state, a bound state is formed, split due to the spin–orbit coupling. The shape of the vibrationally resolved spectra emphasizes considerable prolongation of the Rb–Rb bond

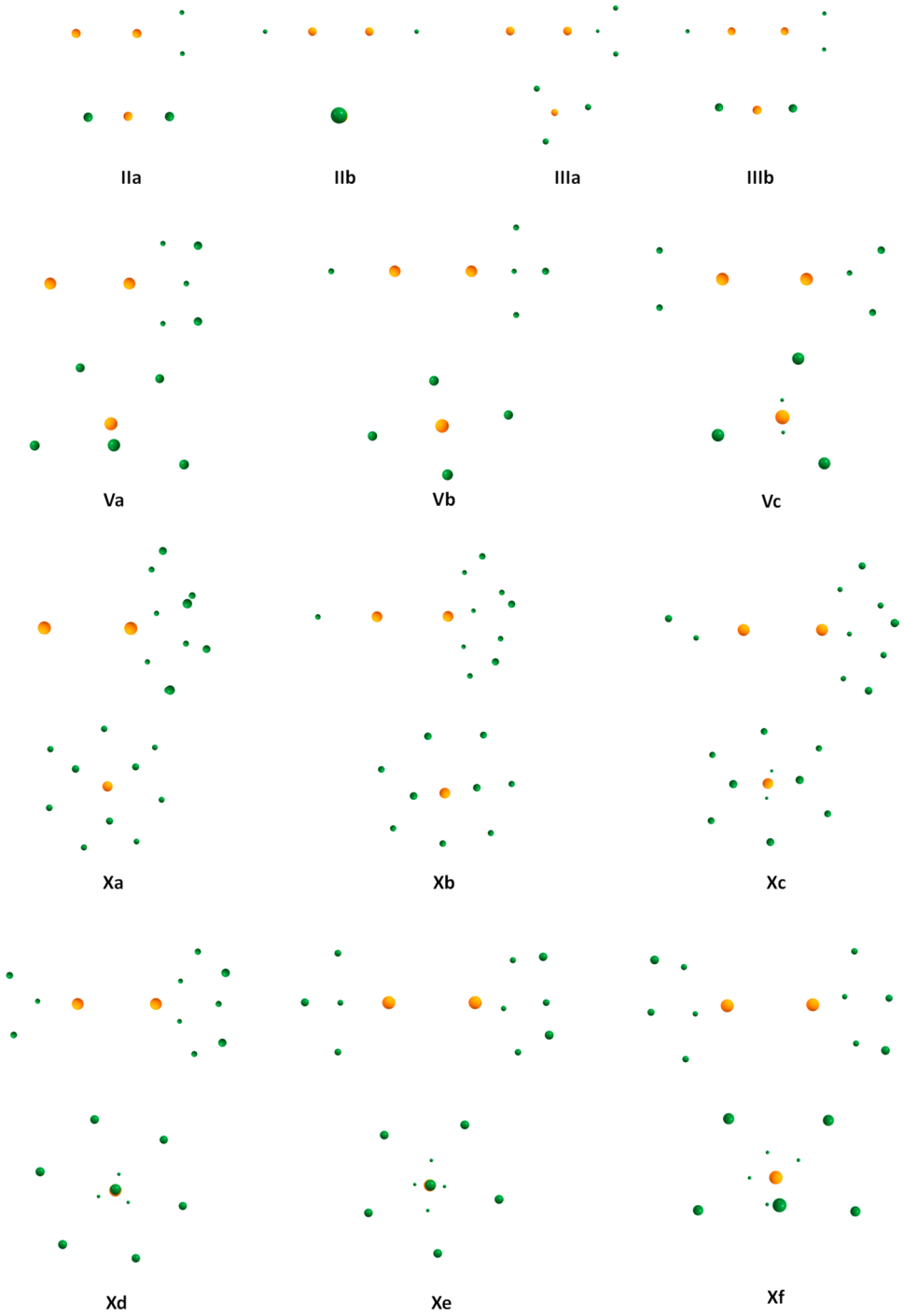

Fig. 7 Selected structures of $He_nRb_2^+$, $n \leq 10$, clusters viewed from the side (above) and along the Rb–Rb axis (below). Optimized at the CCSD(FC)/def2QZVPPD(Rb),def2TZVP(He) level. See Fig. S4 for all optimized structures

in the excited state. The $1^2\Pi_u$ state shifts to slightly lower energies with helium solvation as helium atoms destabilize the ground state more than the final state. While quantum chemical calculations are able to reproduce the spectral shifts qualitatively, predicted values depend considerably on the computational level. For structures with a higher

Table 2 Properties of $He_nRb_2^+$, $n \leq 10$, clusters with different solvation patterns

Isomer	Solv. pattern	E_{solv} [cm^{-1}]	$\Delta E(1^2\Sigma_g^+ - 1^2\Sigma_u^+)$ [cm^{-1}]	$\Delta E(1^2\Sigma_g^+ - 1^2\Pi_u)$ [cm^{-1}]
I	1/0	29	78	−6
IIa	2/0	27	163	−20
IIb	1/1	29	156	−12
IIIa	3/0	25	244	−32
IIIb	2/1	28	244	−26
IVa	4/0	23	324	−38
IVb	3/1	26	330	−38
IVc	2/2	27	336	−40
Va	5/0	22	402	−36
Vb	4/1	24	412	−44
Vc*	3/2	26	424	−51
VIa	6/0	21	486	−41
VIb	5/1	23	493	−43
VIc	4/2	24	511	−57
VId	3/3	25	516	−64
VIIa	7/0	20	526	−35
VIIb	6/1	22	577	−48
VIIc*	5/2	23	594	−56
VIId	4/3	24	605	−69
VIIIa	8/0	19	566	−13
VIIIb	7/1	21	614	−34
VIIIc	6/2	22	636	−45
VIIId	5/3	23	691	−67
VIIIe	4/4	23	696	−74
IXa	9/0	18	585	−1
IXb	8/1	20	661	−19
IXc*	7/2	21	678	−25
IXd	6/3	22	784	−72
IXe	5/4	22	786	−73
Xa	10/0	17	617	20
Xb	9/1	19	681	−7
Xc	8/2	20	769	−32
Xd	7/3	21	829	−66
Xe	6/4	22	882	−77
Xf	5/5	22	879	−71

(*x*/*y* notation denotes *x* He atoms on the one side of Rb_2^+ and *y* on the other.) Solvation energy per helium atom (E_{solv}) and shifts of the vertical excitation energies of the $1^2\Sigma_u^+$ and $1^2\Pi_u$ states with respect to Rb_2^+. Note that the shifts are calculated as a difference of vertical excitation energies. Calculated at the EOMCCSD(FC)/def2QZVPPD//CCSD(FC)/def2QZVPPD(Rb),def2TZVP(He) level. Structures marked with "*" exhibit one small imaginary frequency (< 1 cm^{-1}) that could not be removed by following the respective normal mode

number of adsorbed helium atoms, we predict that He atoms are distributed symmetrically on both sides of the Rb_2^+ ion.

Supplementary Information The online version contains supplementary material available at https://doi.org/10.1007/s00214-021-02728-x.

Acknowledgements SA has received support by the K-Regio project "FAENOMENAL," Project No EFRE 2016-4, funded by the Tyrolean Government and the European Regional Development Fund. The work by PM, AS and OE was supported by the FWF, projects P31149 and I4130. The contribution by EG is part of a project that has received funding from the European Union's Horizon 2020 research and innovation programme under the Marie Skłodowska-Curie grant agreement No. 847476. The views and opinions expressed herein do not necessarily reflect those of the European Commission. The computational results have been achieved using the HPC infrastructure LEO of the University of Innsbruck.

Funding Open access funding provided by University of Innsbruck and Medical University of Innsbruck.

References

1. Thaler B, Ranftl S, Heim P, Cesnik S, Treiber L, Meyer R, Hauser AW, Ernst WE, Koch M (2018) Femtosecond photoexcitation dynamics inside a quantum solvent. Nat Commun 9:4006. https://doi.org/10.1038/s41467-018-06413-9
2. Mauracher A, Echt O, Ellis AM, Yang S, Bohme DK, Postler J, Kaiser A, Denifl S, Scheier P (2018) Cold physics and chemistry: collisions, ionization and reactions inside helium nanodroplets close to zero K. Phys Rep 751:1–90. https://doi.org/10.1016/j.physrep.2018.05.001
3. Gonzalez-Lezana T, Echt O, Gatchell M, Bartolomei M, Campos-Martinez J, Scheier P (2020) Solvation of ions in helium. Int Rev Phys Chem 39:465–516. https://doi.org/10.1080/01442 35X.2020.1794585
4. Castillo-Garcia A, Gonzalez-Lezana T, Delgado-Barrio G, Villarreal P (2018) Formation of rubidium dimers on the surface of helium clusters: a first step through quantum molecular dynamics simulations. Eur Phys J D 72:102. https://doi.org/10.1140/epjd/e2018-90065-3

5. Lehmann KK, Scoles G (1998) Superfluid helium—the ultimate spectroscopic matrix? Science 279:2065–2066. https://doi.org/10.1126/science.279.5359.2065
6. Toennies JP, Vilesov AF (1998) Spectroscopy of atoms and molecules in liquid helium. Ann Rev Phys Chem 49:1–41
7. Yang SF, Ellis AM (2013) Helium droplets: a chemistry perspective. Chem Soc Rev 42:472–484. https://doi.org/10.1039/c2cs35277j
8. Leal A, Mateo D, Hernando A, Pi M, Barranco M, Ponti A, Cargnoni F, Drabbels M (2014) Picosecond solvation dynamics of alkali cations in superfluid ^{4}He nanodroplets. Phys Rev B 90:224518. https://doi.org/10.1103/PhysRevB.90.224518
9. Ancilotto F, DeToffol G, Toigo F (1995) Sodium dimers on the surface of liquid ^{4}He. Phys Rev B 52:16125–16129. https://doi.org/10.1103/PhysRevB.52.16125
10. Stark C, Kresin VV (2010) Critical sizes for the submersion of alkali clusters into liquid helium. Phys Rev B 81:085401. https://doi.org/10.1103/PhysRevB.81.085401
11. An der Lan L, Bartl P, Leidlmair C, Schöbel H, Jochum R, Denifl S, Märk TD, Ellis AM, Scheier P (2011) The submersion of sodium clusters in helium nanodroplets: Identification of the surface → interior transition. J Chem Phys 135:044309. https://doi.org/10.1063/1.3610388
12. Schiller A, Martini P, Maalouf EEJA, Scheier P (2021) Submersion of Rb clusters in helium nanodroplets. Eur Phys J D accepted for publication.
13. Higgins J, Callegari C, Reho J, Stienkemeier F, Ernst WE, Gutowski M, Scoles G (1997) Helium cluster isolation spectroscopy of alkali dimers in the triplet manifold. J Phys Chem A 102:4952–4965. https://doi.org/10.1021/jp981115g
14. Stwalley WC, Bellos M, Carollo R, Banerjee J, Bermudez M (2012) Shortcuts for understanding rovibronic spectroscopy of ultracold alkali metal diatomic molecules. Mol Phys 110:1739–1755. https://doi.org/10.1080/00268976.2012.676680
15. Kubkowska MK, Grochola A, Jastrzebski W, Kowalczyk P (2007) The $C^1\Pi_u$ and $2^1\Sigma_u^+$ states in Li_2: experiment and comparison with theory. Chem Phys 333:214–218. https://doi.org/10.1016/j.chemphys.2007.02.001
16. Grochola A, Jastrzebski W, Kowalczyk P (2008) Spectroscopic study of the $6^1\Pi_u$ state in Li_2. Mol Phys 106:1375–1378. https://doi.org/10.1080/00268970802275595
17. Lackner F, Poms J, Krois G, Pototschnig JV, Ernst WE (2013) Spectroscopy of lithium atoms and molecules on helium nanodroplets. J Phys Chem A 117:11866–11873. https://doi.org/10.1021/jp4030238
18. Wagner GS, Isenor NR (1985) Formation and dissociation of K_2^+, Rb_2^+, and Cs_2^+ ions by ruby laser radiation. Can J Phys 63:976–982. https://doi.org/10.1139/p85-160
19. Arndt PT, Sovkov VB, Ma J, Pan X, Beecher DS, Tsai JY, Guan Y, Lyyra AM, Ahmed EH (2019) Experimental study of the $6^1\Sigma_g^+$ state of the rubidium dimer. Phys Rev A 99:052511. https://doi.org/10.1103/PhysRevA.99.052511
20. Musial M, Kucharski SA (2014) First principle calculations of the potential energy curves for electronic states of the lithium dimer. J Chem Theory Comput 10:1200–1211. https://doi.org/10.1021/ct401076e
21. Chung HK, Kirby K, Babb JF (2001) Theoretical study of the absorption spectra of the sodium dimer. Phys Rev A. https://doi.org/10.1103/PhysRevA.63.032516
22. Valance A (1978) Adiabatic potential energies for NaK^+, $NaRb^+$, $NaCs^+$, KRb^+, KCs^+, $RbCs^+$, Na_2^+, K_2^+, Rb_2^+, and Cs_2^+ molecular ions. J Chem Phys 69:355–366. https://doi.org/10.1063/1.436361
23. Jraij A, Allouche AR, Magnier S, Aubert-Frecon M (2008) Theoretical spin-orbit structure of the alkali dimer cation K_2^+. Can J Phys 86:1409–1415. https://doi.org/10.1139/p08-091
24. Partridge H, Dixon DA, Walch SP, Bauschlicher CW, Gole JL (1983) Electron affinities of the alkali dimers: Na_2, K_2, and Rb_2. J Chem Phys 79:1859–1865. https://doi.org/10.1063/1.445962
25. Müller W, Meyer W (1984) Ground-state properties of alkali dimers and their cations (including the elements Li, Na, and K) from *ab initio* calculations with effective core polarization potentials. J Chem Phys 80:3311–3320. https://doi.org/10.1063/1.447084
26. Fernandez Serra P, Botella V, Smeyers YG (1995) Ground-state and some excited states of Li_2 by the half-projected Hartree–Fock method. Int J Quantum Chem 54:305–311. https://doi.org/10.1002/qua.560540506
27. Andriopoulos N, Vonnagyfelsobuki EI (1988) Pseudopotential calculations for Li_2, Na_2 and NaLi. Aust J Phys 41:563–572. https://doi.org/10.1071/ph880563
28. Chu SY (1972) SCF calculations for H_2^+, Li_2^+ and LiH^+ with atomic basis sets enlarged by bond functions. Theor Chim Acta 25:200–204. https://doi.org/10.1007/bf01135646
29. Magnier S, Millie P, Dulieu O, Masnouseeuws F (1993) Potential curves for the ground and excited states of the Na_2 molecule up to the (3*s*+5*p*) dissociation limit: results of two different effective potential calculations. J Chem Phys 98:7113–7125. https://doi.org/10.1063/1.464755
30. Gabbanini C (2007) Formation, detection and trapping of ultracold Rb_2 molecules. Nucl Phys A 790:757C-761C. https://doi.org/10.1016/j.nuclphysa.2007.03.022
31. Lee YT, Mahan BH (1965) Photosensitized ionization of alkali-metal vapors. J Chem Phys 42:2893–2896. https://doi.org/10.1063/1.1703258
32. Olson RE (1969) Determination of the difference potential from resonant charge-exchange total cross sections: analysis of Rb^+-Rb and Cs^+-Cs. Phys Rev 187:153–161. https://doi.org/10.1103/PhysRev.187.153
33. Bellomonte L, Cavaliere P, Ferrante G (1974) Alkali molecular ion energies and expectation values in a model-potential treatment. J Chem Phys 61:3225–3229. https://doi.org/10.1063/1.1682480
34. Jraij A, Allouche AR, Korek M, Aubert-Frecon M (2003) Theoretical electronic structure of the alkali-dimer cation Rb_2^+. Chem Phys 290:129–136. https://doi.org/10.1016/s0301-0104(03)00060-0
35. Aymar M, Azizi S, Dulieu O (2003) Model-potential calculations for ground and excited Σ states of Rb_2^+, Cs_2^+ and $RbCs^+$ ions. J Phys B 36:4799–4812. https://doi.org/10.1088/0953-4075/36/24/004
36. Klapisch M (1971) A program for atomic wavefunction computations by the parametric potential method. Comput Phys Commun 2:239–260. https://doi.org/10.1016/0010-4655(71)90001-4
37. Smialkowski M, Tomza M (2020) Interactions and chemical reactions in ionic alkali-metal and alkaline-earth-metal diatomic AB^+ and triatomic A_2B^+ systems. Phys Rev A 101:012501. https://doi.org/10.1103/PhysRevA.101.012501
38. Silberbach H, Schwerdtfeger P, Stoll H, Preuss H (1986) Ground and excited states of Rb_2^+ and Cs_2^+ by means of quasi-relativistic pseudo-potentials including core polarisation. J Phys B 19:501–510. https://doi.org/10.1088/0022-3700/19/5/011
39. Krauss M, Stevens WJ (1990) Effective core potentials and accurate energy curves for Cs_2 and other alkali diatomics. J Chem Phys 93:4236–4242. https://doi.org/10.1063/1.458756
40. Patil SH, Tang KT (2000) Simple model potential and model wave functions for $(H\text{-alkali})^+$ and $(alkali\text{-}alkali)^+$ ions. J Chem Phys 113:676–682. https://doi.org/10.1063/1.481843
41. Lim IS, Schwerdtfeger P, Sohnel T, Stoll H (2005) Ground-state properties and static dipole polarizabilities of the alkali dimers from K_2^n to Fr_2^n (n=0,+1) from scalar relativistic pseudopotential coupled cluster and density functional studies. J Chem Phys 122:134307. https://doi.org/10.1063/1.1869979

42. Jyothi S, Ray T, Dutta S, Allouche AR, Vexiau R, Dulieu O, Rangwala SA (2016) Photodissociation of trapped Rb_2^+: implications for simultaneous trapping of atoms and molecular ions. Phys Rev Lett 117:213002. https://doi.org/10.1103/PhysRevLett.117.213002
43. Rakic M, Pichler G (2018) Photoionization bands of rubidium molecule. J Quant Spectrosc Radiat Transfer 208:39–44. https://doi.org/10.1016/j.jqsrt.2018.01.003
44. Helm H, Cosby PC, Huestis DL (1983) Observation of the $1^2\Pi_u \leftarrow X^2\Sigma_g^+$ system in Cs_2^+. J Chem Phys 78:6451–6454. https://doi.org/10.1063/1.444683
45. Kranabetter L, Bersenkowitsch NK, Martini P, Gatchell M, Kuhn M, Laimer F, Schiller A, Beyer MK, Ončák M, Scheier P (2019) Considerable matrix shift in the electronic transitions of helium-solvated cesium dimer cation $Cs_2He_n^+$. Phys Chem Chem Phys 21:25362–25368. https://doi.org/10.1039/c9cp04790e
46. Honig RE, Kramer DA (1969) Vapor pressure data for solid and liquid elements. RCA Rev 30:285
47. Koch H, Jorgensen P (1990) Coupled cluster response functions. J Chem Phys 93:3333–3344. https://doi.org/10.1063/1.458814
48. Stanton JF, Bartlett RJ (1993) The equation of motion coupled-cluster method. A systematic biorthogonal approach to molecular excitation energies, transition probabilities, and excited state properties. J Chem Phys 98:7029–7039. https://doi.org/10.1063/1.464746
49. Krylov AI (2008) Equation-of-motion coupled-cluster methods for open-shell and electronically excited species: the Hitchhiker's guide to Fock space. Ann Rev Phys Chem 59:433–462. https://doi.org/10.1146/annurev.physchem.59.032607.093602
50. Werner HJ, Knowles PJ (1988) An efficient internally contracted multiconfiguration–reference configuration interaction method. J Chem Phys 89:5803–5814. https://doi.org/10.1063/1.455556
51. Knowles PJ, Werner HJ (1988) An efficient method for the evaluation of coupling coefficients in configuration interaction calculations. Chem Phys Lett 145:514–522. https://doi.org/10.1016/0009-2614(88)87412-8
52. Lim IS, Schwerdtfeger P, Metz B, Stoll H (2005) All-electron and relativistic pseudopotential studies for the group 1 element polarizabilities from K to element 119. J Chem Phys 122:104103. https://doi.org/10.1063/1.1856451
53. Werner H-J, Knowles PJ, Knizia G, Manby FR, Schuetz M (2012) MOLPRO: a general-purpose quantum chemistry program package. Wiley Interdiscip Rev Comput Mol Sci 2:242–253. https://doi.org/10.1002/wcms.82
54. Noro T, Sekiya M, Koga T (2012) Segmented contracted basis sets for atoms H through Xe: Sapporo-(DK)-*n*ZP sets (n = D, T, Q). Theor Chem Acc 131:1124. https://doi.org/10.1007/s00214-012-1124-z
55. Kramida A, Ralchenko Yu, Reader J and NIST ASD Team (2020). NIST Atomic Spectra Database (version 5.8), [Online]. https://physics.nist.gov/asd [Mon Nov 28 2020]. https://doi.org/10.18434/T4W30F
56. Ončák M, Šištík L, Slavíček P (2010) Can theory quantitatively model stratospheric photolysis? Ab initio estimate of absolute absorption cross sections of ClOOCl. J Chem Phys 133:174303. https://doi.org/10.1063/1.3499599
57. Lee SY, Brown RC, Heller EJ (1983) Multidimensional reflection approximation: application to the photodissociation of polyatomics. J Phys Chem 87:2045–2053. https://doi.org/10.1021/j100235a006
58. Prakash MK, Weibel JD, Marcus RA (2005) Isotopomer fractionation in the UV photolysis of N_2O: Comparison of theory and experiment. J Geophys Res: Atmos 110:D21315. https://doi.org/10.1029/2005jd006127
59. Frisch MJ, Trucks GW, Schlegel HB, Scuseria GE, Robb MA, Cheeseman JR, Scalmani G, Barone V, Petersson GA, Nakatsuji H, Li X, Caricato M, Marenich AV, Bloino J, Janesko BG, Gomperts R, Mennucci B, Hratchian HP, Ortiz JV, Izmaylov AF, Sonnenberg JL, Williams, Ding F, Lipparini F, Egidi F, Goings J, Peng B, Petrone A, Henderson T, Ranasinghe D, Zakrzewski VG, Gao J, Rega N, Zheng G, Liang W, Hada M, Ehara M, Toyota K, Fukuda R, Hasegawa J, Ishida M, Nakajima T, Honda Y, Kitao O, Nakai H, Vreven T, Throssell K, Montgomery Jr. JA, Peralta JE, Ogliaro F, Bearpark MJ, Heyd JJ, Brothers EN, Kudin KN, Staroverov VN, Keith TA, Kobayashi R, Normand J, Raghavachari K, Rendell AP, Burant JC, Iyengar SS, Tomasi J, Cossi M, Millam JM, Klene M, Adamo C, Cammi R, Ochterski JW, Martin RL, Morokuma K, Farkas O, Foresman JB, Fox DJ (2016) Gaussian 16 Rev. A.03. Wallingford, CT
60. Svoboda O, Hollas D, Ončák M, Slavíček P (2013) Reaction selectivity in an ionized water dimer: nonadiabatic ab initio dynamics simulations. Phys Chem Chem Phys 15:11531–11542. https://doi.org/10.1039/c3cp51440d
61. Western CM (2017) PGOPHER: A program for simulating rotational, vibrational and electronic spectra. J Quant Spectrosc Radiat Transfer 186:221–242. https://doi.org/10.1016/j.jqsrt.2016.04.010
62. Marinetti F, Uranga-Pina LI, Coccia E, Loopez-Duran D, Bodo E, Gianturco FA (2007) Microsolvation of cationic dimers in ^{4}He droplets: geometries of $A_2^+(He)_N$ (A = Li, Na, K) from optimized energies. J Phys Chem A 111:12289–12294. https://doi.org/10.1021/jp0748361